# FDFD: A 3D Finite-Difference Frequency-Domain Code for Electromagnetic Induction Tomography [1]

Nathan J. Champagne II, James G. Berryman, and H. Michael Buettner

*Lawrence Livermore National Laboratory, Livermore, CA 94550*

A new 3D code for ElectroMagnetic Induction Tomography (EMIT) with intended applications to environmental imaging problems has been developed. The approach consists of calculating the fields within a volume using an implicit finite-difference frequency-domain (FDFD) formulation. The volume is terminated by an anisotropic perfectly matched layer (PML) region that simulates an infinite domain by absorbing outgoing waves. Extensive validation of this code has been done using analytical and semianalytical results from other codes and some of those results are presented in this paper. The new code is written in Fortran 90 and is designed to be easily parallelized, but this feature has yet to be tested. Finally, an adjoint method, developed for solving the inverse problem for conductivity imaging (for mapping underground plumes), uses this code as its forward field solver.

## 1. INTRODUCTION

Although electromagnetic surveying techniques of both the electrical current injection type and the magnetic field type have been well-known for many years [1], efforts to turn these surveys into true 3D maps of subsurface physical properties have only been attempted in the last 10 to 20 years [2], [3]. One of the reasons for this delay has surely been the necessity of using large computer memories and fast computing machines, because it does not take a very large 3D forward modeling problem to swamp even today's most advanced computing platforms. A recent review of the state of the art in 3D EM modeling [4] demonstrated the limitations and lack of consensus on the best methods for computing EM fields in applications to inhomogeneous earth materials.

In this context, we have developed and continue to test and improve a new 3D code for application to electromagnetic induction tomography and to environmental imaging problems. The finite-difference frequency-domain formulation is based on

[1] This work was performed under the auspices of the U.S. Department of Energy by the Lawrence Livermore National Laboratory under contract No. W-7405-ENG-48 and supported specifically by the Environmental Management Science Program of the Office of Environmental Management and the Office of Energy Research.

that in [5], and an anisotropic perfectly matched layer approach [6], [7] is used to specify the boundary conditions. The present paper summarizes our progress to date on this code development.

Section 2 describes the algorithm implemented in the code. Section 3 provides a series of examples validating the code. And Section 4 discusses how the code will be used in the inversion problem for ElectroMagnetic Induction Tomography.

## 2. FDFD ALGORITHM

The goal of this code development effort is to produce an accurate and efficient forward simulation for EM fields that can then be easily used for inversion of ElectroMagnetic Induction Tomography (EMIT) field data. The FDFD (finite-difference frequency-domain) formulation presented here is an extension to lossy media of a method developed for lossless media in [5]. The mesh truncation approach involves using an anisotropic absorbing PML (perfectly matched layer) following the ideas in [6], [8]. The absorbing regions have material parameters similar to those proposed in [9]. The code is written in Fortran 90, and ease of portability to various high performance computing platforms has been one of our design criteria throughout its development.

### 2.1. Finite-difference, frequency-domain formulation

To develop a system of equations to determine the electric and magnetic fields within a volume, the integral form of Maxwell's curl equations (Ampère's and Faraday's laws),

$$\oint_C \mathbf{H} \cdot d\boldsymbol{\ell} = j\omega \int_S (\overline{\boldsymbol{\epsilon}} \cdot \mathbf{E}) \cdot \widehat{\mathbf{n}}\, dS + \int_S \mathbf{J} \cdot \widehat{\mathbf{n}}\, dS \tag{1}$$

and

$$\oint_C \mathbf{E} \cdot d\boldsymbol{\ell} = -j\omega \int_S (\overline{\boldsymbol{\mu}} \cdot \mathbf{H}) \cdot \widehat{\mathbf{n}}\, dS - \int_S \mathbf{M} \cdot \widehat{\mathbf{n}}\, dS, \tag{2}$$

are used. Here $\mathbf{J}$ is the impressed electric current density, $\mathbf{M}$ is the impressed magnetic current density, $\overline{\boldsymbol{\epsilon}}$ and $\overline{\boldsymbol{\mu}}$ are diagonal dyads of dielectric permittivity and magnetic permeability respectively, and $C$ is the boundary of the open surface $S$. The integrals in (1) and (2) are applied to discrete elements (rectangular blocks) within the volume using the following relations:

$$\int_{-a/2}^{a/2} \mathbf{f} \cdot d\boldsymbol{\ell} \rightarrow a f_m \tag{3}$$

and

$$\int_{-a/2}^{a/2} \int_{-b/2}^{b/2} \mathbf{f} \cdot \widehat{\mathbf{n}}\, dS \rightarrow ab f_m, \tag{4}$$

where $f_m$ is a center value associated with the $m$th cell shown in Fig. 1. Note that the discrete electric field is located at the center of an edge and the discrete magnetic field flows through the centroid of a face. Also, the $m$th cell is normally referred

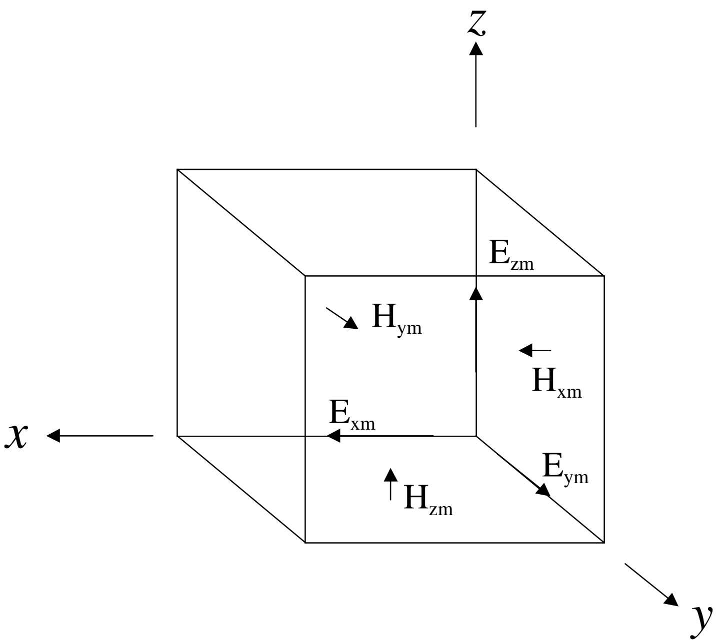


**FIG. 1.** The field quantities associated with the $m$th cell $(i,j,k)$.

to as cell$(i, j, k)$, but for notational convenience, a cell mapping using symbols such as $u, d, l, r, f, b$ (for up, down, left, right, front, back) to specify the six cells surrounding the $m$th cell is used. This mapping is presented in Table 1. Cells other than the six cells adjacent to the six faces may also be labelled using the same mapping. For example, relative to cell $m$, cell *df* is cell$(i-1, j, k-1)$ and cell *dlb* is cell$(i-1, j-1, k+1)$.

**TABLE 1**
**Labels for cells surrounding $\boldsymbol{m} =$ cell$(\boldsymbol{i}, \boldsymbol{j}, \boldsymbol{k})$.**

| | |
|---|---|
| $d =$ cell$(i-1, j, k)$ | $u =$ cell$(i+1, j, k)$ |
| $l =$ cell$(i, j-1, k)$ | $r =$ cell$(i, j+1, k)$ |
| $f =$ cell$(i, j, k-1)$ | $b =$ cell$(i, j, k+1)$ |

The discretized form of (1) and (2) results in an equation for each field component. The resulting equations are cumbersome; however, presenting each expression using matrices provides a compact form. Thus, using quantities defined in the Appendix, (1) and (2) become

$$\boldsymbol{A}^T \boldsymbol{D}_{\bar{\ell}}\, \vec{h} = j\omega\epsilon_0 \boldsymbol{D}_{A\epsilon}\, \vec{e} + \boldsymbol{D}_{\bar{A}}\, \vec{j} \tag{5}$$

and

$$\boldsymbol{A}\boldsymbol{D}_{\ell}\,\vec{e} = -j\omega\mu_0\boldsymbol{D}_{A}\,\boldsymbol{D}_{\mu}\,\vec{h} - \boldsymbol{D}_{A}\,\vec{m}, \tag{6}$$

respectively. The apparent lack of symmetry in the pair of equations (5) and (6) arises from differences in the method of discretizing $\epsilon$ and $\mu$ on the staggered grid (see the Appendix for the details). Solving for the magnetic field (in order to eliminate it from the equations) in (6) and then substituting the result into (5) yields

$$\begin{aligned} \boldsymbol{A}^T\boldsymbol{D}_{\bar{\ell}}\,\boldsymbol{D}_{\mu}^{-1}\,\boldsymbol{D}_{A}^{-1}\,\boldsymbol{A}\boldsymbol{D}_{\ell}\,\vec{e} - k_0^2\boldsymbol{D}_{A\epsilon}\,\vec{e} = \\ -j\omega\mu_0\boldsymbol{D}_{\bar{A}}\,\vec{j} - \boldsymbol{A}^T\boldsymbol{D}_{\bar{\ell}}\,\boldsymbol{D}_{\mu}^{-1}\,\vec{m}, \end{aligned} \tag{7}$$

which has a form entirely analogous to that commonly used in finite element codes, *i.e.*,

$$\begin{aligned} \boldsymbol{\nabla}\times\left(\overline{\boldsymbol{\mu}}_r^{-1}\cdot\boldsymbol{\nabla}\times\mathbf{E}\right) - k_0^2\overline{\boldsymbol{\epsilon}}_r\cdot\mathbf{E} = \\ -j\omega\mu_0\mathbf{J} - \boldsymbol{\nabla}\times\overline{\boldsymbol{\mu}}_r^{-1}\cdot\mathbf{M}, \end{aligned} \tag{8}$$

even though our goal here is to develop a finite difference code.

A commonly observed problem in numerical computations of Maxwell's equations arises due to a possible resonance at zero frequency. If this occurs, the resulting matrix has an eigenvalue at zero and therefore is not positive definite and not invertible. For the geometries considered here, the fields for resonant frequency of 0 Hz are generated only by electric charge within the volume. Such charges may develop as an artifact of numerical roundoff when evaluating the vector wave equation — especially at lower frequencies. This problem is avoided by eliminating any charge within the volume using a term analogous to

$$\boldsymbol{\nabla}\left[\boldsymbol{\nabla}\cdot(\overline{\boldsymbol{\epsilon}}_r\cdot\mathbf{E})\right] = \mathbf{0}. \tag{9}$$

This is achieved by starting from Gauss's law for the electric field in integral form,

$$\int_V \boldsymbol{\nabla}\cdot(\overline{\boldsymbol{\epsilon}}_r\cdot\mathbf{E})\,dV = \oint_S(\overline{\boldsymbol{\epsilon}}_r\cdot\mathbf{E})\cdot\widehat{\mathbf{n}}\,dS = 0, \tag{10}$$

to arrive at the discretized matrix expression

$$\left[\boldsymbol{D}_{\ell}^{-1}\boldsymbol{D}_{A\epsilon}^{*}\boldsymbol{B}^T\left(\boldsymbol{D}_{V\epsilon\epsilon}^{-1}\boldsymbol{B}\boldsymbol{D}_{A\epsilon}\right)\right]\vec{e} = \vec{0}, \tag{11}$$

where the matrices in parenthesis arise from discretizing (10) while the remaining matrices in the square bracket arise from discretizing (9) after the application of an integral identity. When (11) is added to (7), the result is

$$\begin{aligned} (\boldsymbol{A}^T\boldsymbol{D}_{\bar{\ell}}\,\boldsymbol{D}_{\mu}^{-1}\,\boldsymbol{D}_{A}^{-1}\,\boldsymbol{A}\boldsymbol{D}_{\ell} + \boldsymbol{D}_{\ell}^{-1}\boldsymbol{D}_{A\epsilon}^{*}\boldsymbol{B}^T\boldsymbol{D}_{V\epsilon\epsilon}^{-1}\boldsymbol{B}\boldsymbol{D}_{A\epsilon} \\ -k_0^2\boldsymbol{D}_{A\epsilon})\vec{e} = -j\omega\mu_0\boldsymbol{D}_{\bar{A}}\,\vec{j} - \boldsymbol{A}^T\boldsymbol{D}_{\bar{\ell}}\,\boldsymbol{D}_{\mu}^{-1}\,\vec{m}. \end{aligned} \tag{12}$$

However, a more symmetric form is obtained by multiplying through by $\boldsymbol{D}^{1/2}$ and then rewriting (12) as

$$(\boldsymbol{D}_{\ell}^{1/2}\boldsymbol{A}^T\boldsymbol{D}_{\bar{\ell}}\,\boldsymbol{D}_{\mu}^{-1}\,\boldsymbol{D}_{A}^{-1}\,\boldsymbol{A}\boldsymbol{D}_{\ell}^{1/2} +$$

$$\begin{aligned}\boldsymbol{D}_\ell^{-1/2}\boldsymbol{D}_{A\epsilon}^{*}\boldsymbol{B}^T\boldsymbol{D}_{V\epsilon\epsilon}^{-1}\boldsymbol{B}\boldsymbol{D}_{A\epsilon}\boldsymbol{D}_\ell^{-1/2} - k_0^2\boldsymbol{D}_{A\epsilon})\boldsymbol{D}_\ell^{1/2}\vec{e} = \\ -j\omega\mu_0\boldsymbol{D}_\ell^{1/2}\boldsymbol{D}_{\bar{A}}\,\vec{j} - \boldsymbol{D}_\ell^{1/2}\boldsymbol{A}^T\boldsymbol{D}_{\bar{\ell}}\,\boldsymbol{D}_\mu^{-1}\,\vec{m}.\end{aligned} \tag{13}$$

### 2.2. PML formulation for mesh truncation

The mesh is truncated using perfectly matched layers (PML) that absorb electromagnetic waves following the general ideas in [6]. The PML is a representation of anisotropic media satisfying

$$\mathbf{D} = \overline{\boldsymbol{\epsilon}}_{\text{PML}} \cdot \mathbf{E} \qquad \text{and} \qquad \mathbf{B} = \overline{\boldsymbol{\mu}}_{\text{PML}} \cdot \mathbf{H}, \tag{14}$$

where

$$\overline{\boldsymbol{\epsilon}}_{\text{PML}} = \overline{\boldsymbol{\epsilon}} \cdot \overline{\boldsymbol{\Lambda}} \qquad \text{and} \qquad \overline{\boldsymbol{\mu}}_{\text{PML}} = \overline{\boldsymbol{\mu}} \cdot \overline{\boldsymbol{\Lambda}}. \tag{15}$$

The symbol $\overline{\boldsymbol{\Lambda}}$ stands for a diagonal dyad that has entries selected to absorb incident electromagnetic waves. The form of this dyadic quantity is determined by the normal to the PML interface. As an example, for a PML interface with a normal in the $z$ direction, the form of $\overline{\boldsymbol{\Lambda}}$ is given by [7], [9]

$$\overline{\boldsymbol{\Lambda}}_z = \begin{bmatrix} a & 0 & 0 \\ 0 & a & 0 \\ 0 & 0 & 1/a \end{bmatrix}, \tag{16}$$

in which $a$ is given by

$$a = 1 + \frac{f(x,y,z)}{1 + j\alpha\omega}, \tag{17}$$

where $\alpha$ is a constant and $f(x,y,z)$ is a function of position that falls to zero at the interface between the modeling space and the desired PML boundary. We have found through empirical studies that a suitable form for $a$ is

$$a = 1 + \frac{f(x,y,z)}{1 + j\epsilon_0\omega}, \tag{18}$$

where $f(x,y,z)$ is given by

$$f(x,y,z) = \frac{(1-j)\,\beta}{\rho(x,y,z)}. \tag{19}$$

Here, $\rho(x,y,z)$ is a discretized distance from the modeling space/PML interface to the centroid of the cell of interest inside the PML. The parameter $\beta$ is chosen to fix the amplitude of $f(x,y,z)$. To date, the best form of $\rho(x,y,z)$ has been found to be linear in the distance as determined by numerical experimentation so that $f(x,y,z)$ has an inverse type distribution like that in [11], [12].

## 3. EXAMPLES

To demonstrate the accuracy and convergence properties of the code FDFD (for finite-difference/frequency-domain), we have tested various cases against analytical

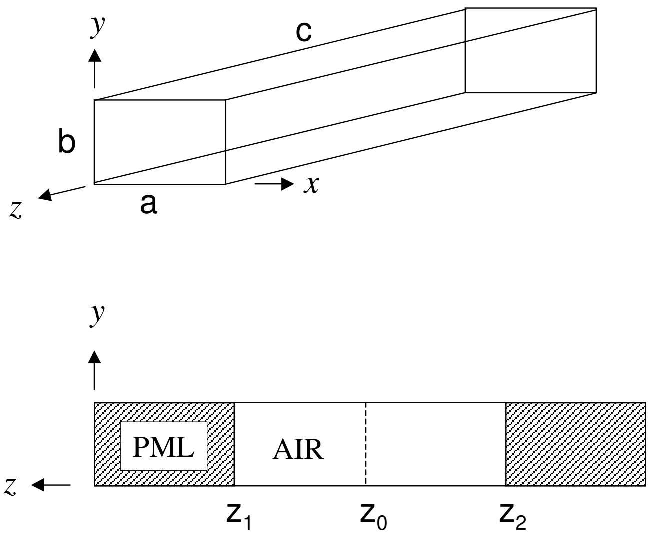


**FIG. 2.** A rectangular cavity with dimensions $a = 80$ m, $b = 5$ m, and $c = 400$ m. Also, $Z_0 = -200$ m, $Z_1 = -100$ m, and $Z_2 = -300$ m. The frequency of operation is 2 MHz.

and semianalytical results. The set of results include 1D, 2D, and 3D example problems.

A rectangular cavity (80 m × 5 m × 400 m) is shown in Fig. 2. There are 16 cells in the $x$ direction, 1 cell in the $y$ direction, and 80 cells in the $z$ direction. The frequency of operation is 2 MHz, and the air/PML interfaces are located at $Z_1 = -100$ m and $Z_2 = -300$ m. The dominant ($TE_{101}$) mode of the cavity is launched from $Z_0 = -200$ m. The magnitude and phase of $E_y$, sampled at $x = 40$ m, are shown in Figs. 3 and 4. The FDFD results agree well with analytical calculations, with the only significant deviations lying within the PML regions.

A line of constant current is placed in the center of the square cavity shown in Fig. 5. Each side has a length of 400 m (80 cells), and the height of the cavity is 5 m (1 cell). The frequency of operation is 2 MHz. The magnitude and phase of $E_z$ are shown in Figs. 6 and 7. The data are plotted as a function of $\rho$, which is positive when to the right of the line source or negative if to the left. The calculated and analytical data agree well, with the only significant deviations occurring in the PML region.

The two sets of 3D examples we will show here are based on the field geometry of Fig. 8. Receivers are down a borehole in a layered medium with air above the free surface. The first example of a buried resistive layer has a 60 m thick layer with conductivity = 0.3 S/m, a 25 m thick layer with conductivity = 0.016 S/m, and an 85 m layer with conductivity = 0.3 S/m at the bottom of the model. Appropriately designed PML absorbing layers surround the modeled region on all six sides of the domain. The relative permittivity of all three earth layers is constant and assumed to equal 10.0. The frequency of the excitation is 1 kHz with the magnetic dipole transmitter located at the free surface with an offset of 5 m from the borehole. The finite difference representation was chosen so the unit spacing in the earth model

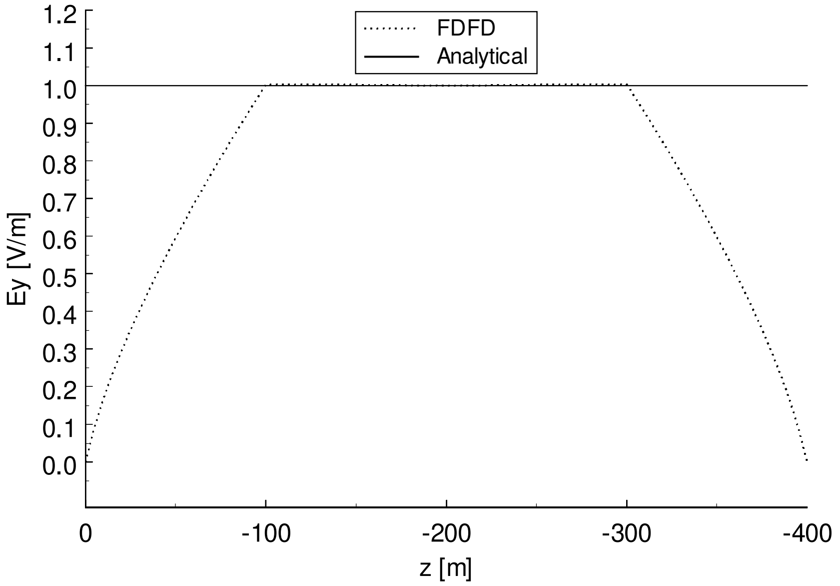


**FIG. 3.** The magnitude of $E_y$ at $x = 40\ m$ for the rectangular cavity.

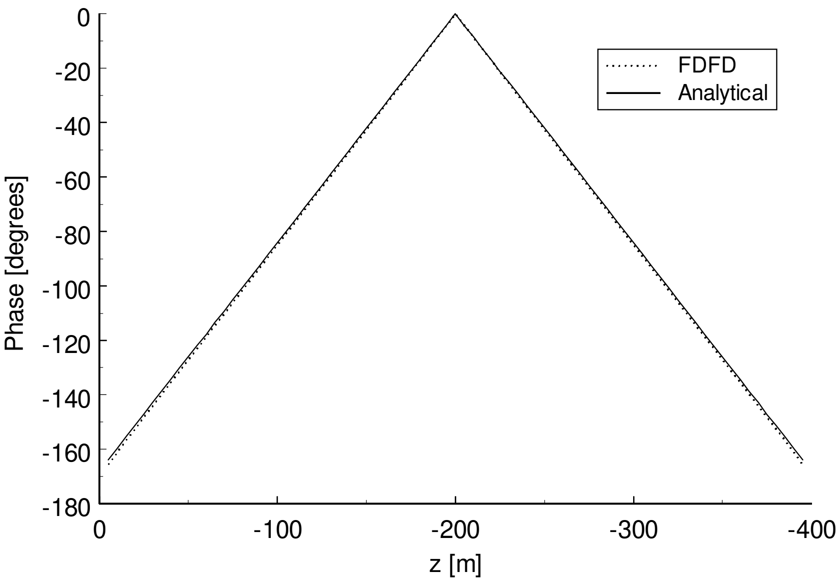


**FIG. 4.** The phase of $E_y$ at $x = 40\ m$ for the rectangular cavity.

was 2.5 m, with 50 cells $\times$ 50 cells in the $xy$ direction, and 10 layers of PML on those four sides. In the vertical direction, there were 68 cells in the earth model, 12 cells in the air above the free surface, and 10 more cells above and below for the PML layers. All PML cells are 10m thick in the directions away from the earth model. The overall problem is then approximately $70 \times 70 \times 100 \simeq 500,000$ cells. The computations were performed on a DEC Digital Ultimate Workstation (533 MHz) and required approximately 45 minutes of CPU time using about 260 iterations to achieve the convergence for the largest choice of tolerance ($10^{-5}$). The smallest tolerance ($10^{-7}$) required about 3.4 hours and 1200 iterations. This computation was serial and required about 700 MB of memory. In Figs. 9 and 10 the results of the code calculations for the magnetic field magnitude and phase are compared to results for the same model obtained using the code EM1D (based on a semianalytical formula for such layered models) developed by Ki-Ha Lee at LBNL. The observed agreement is good for all choices of convergence tolerance, but becomes excellent for the two smallest values.

Since the buried resistive layer might be viewed as an easy case for the PML since the majority of the medium is conducting and therefore helping to attenuate the signal — perhaps obviating the need for the PML, we have also tested the code for the reverse problem of a buried conductive layer in a resistive background. All the

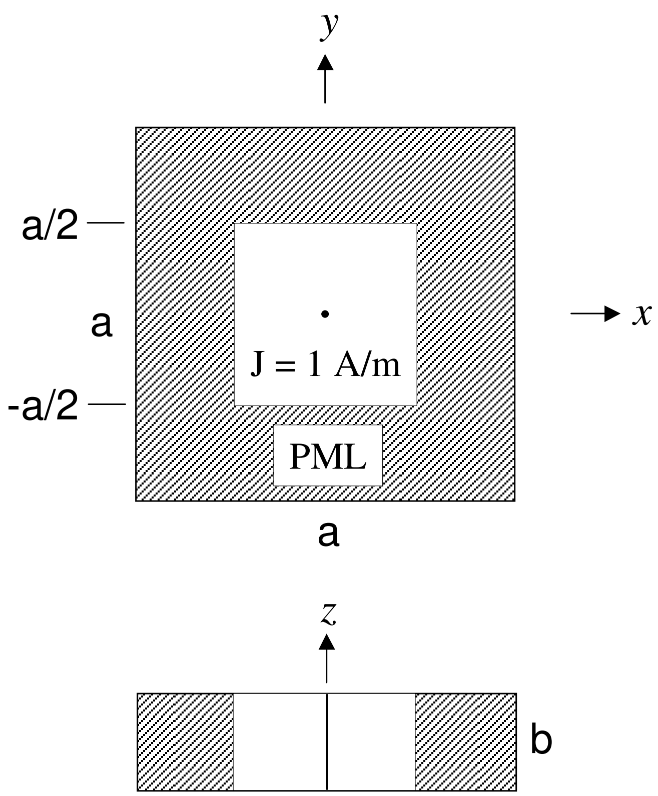


**FIG. 5.** A square cavity with dimensions $a = 400$ m and $b = 5$ m. The line of current is along the $z$ axis. The frequency of operation is 2 MHz.

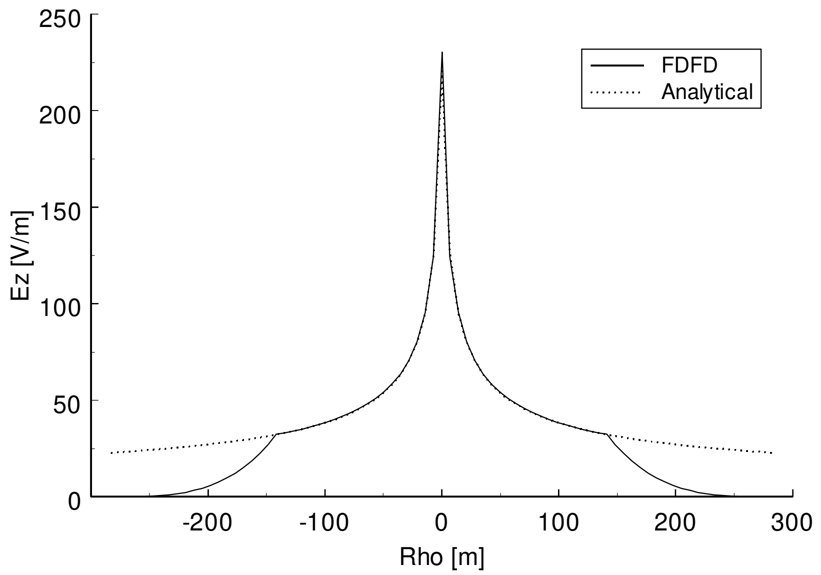


**FIG. 6.** The magnitude of $E_z$ for the square cavity.

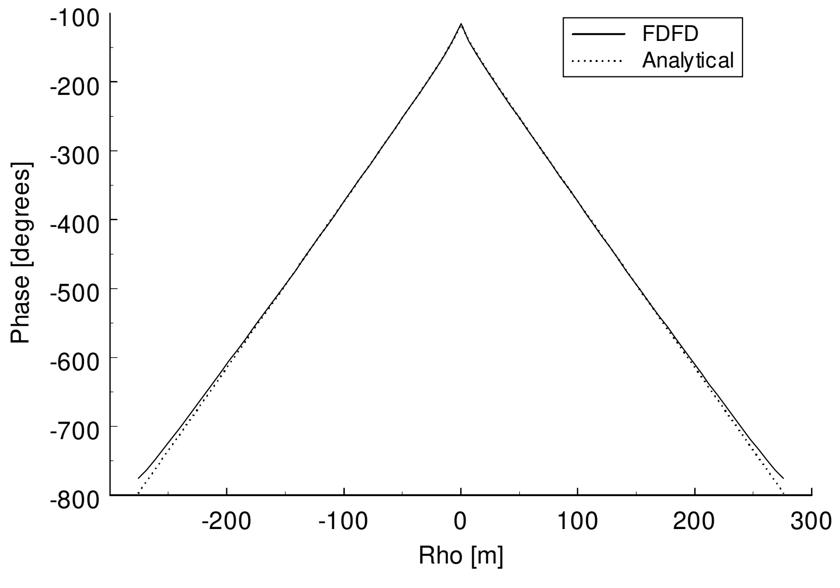


**FIG. 7.** The phase of $E_z$ for the square cavity.

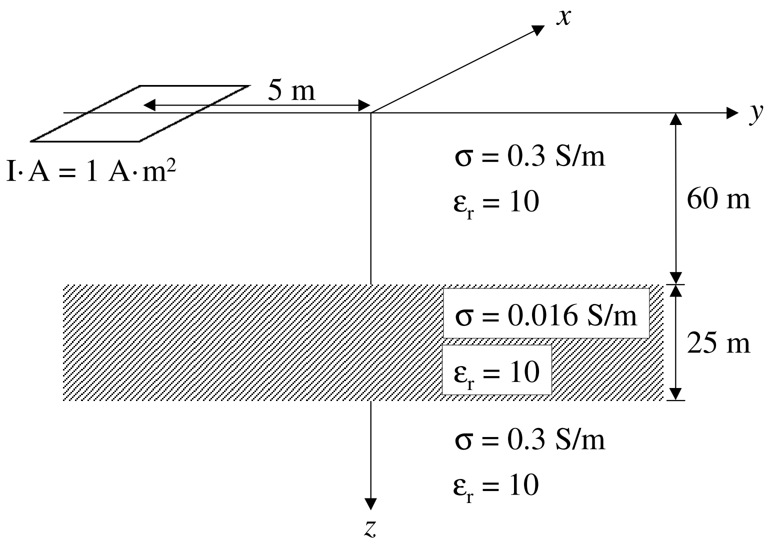


**FIG. 8.** Current loop at the surface of medium with a buried resistive layer. The same basic picture also applies to our second example with a buried conducting layer, but the conductivity values are reversed ($0.3 \leftrightarrow 0.016$) in that case.

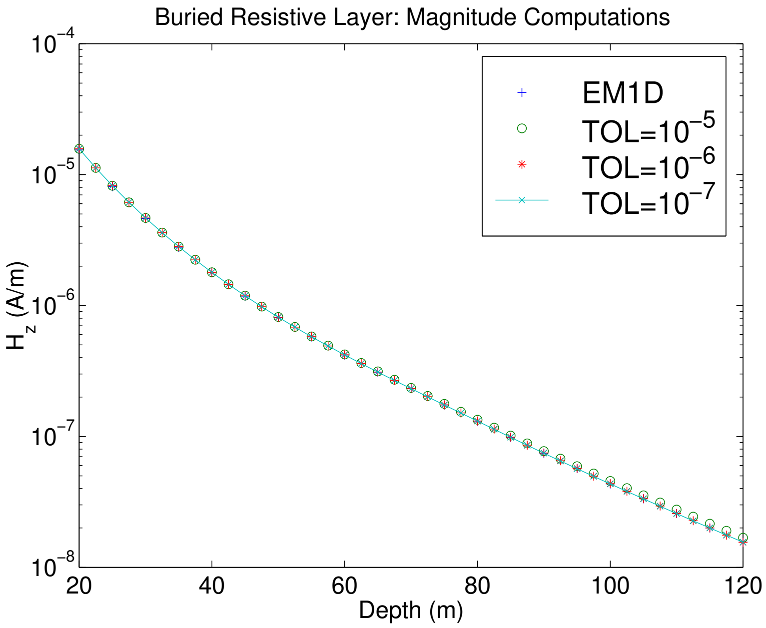


**FIG. 9.** Comparison of FDFD computed magnitude of magnetic field in the layered model with buried resistive layer in Fig. 8 with semianalytic results from EM1D of Ki-Ha Lee (LBNL). The two smaller choices of convergence tolerance give virtually the same results for this example, and are in good agreement with EM1D.

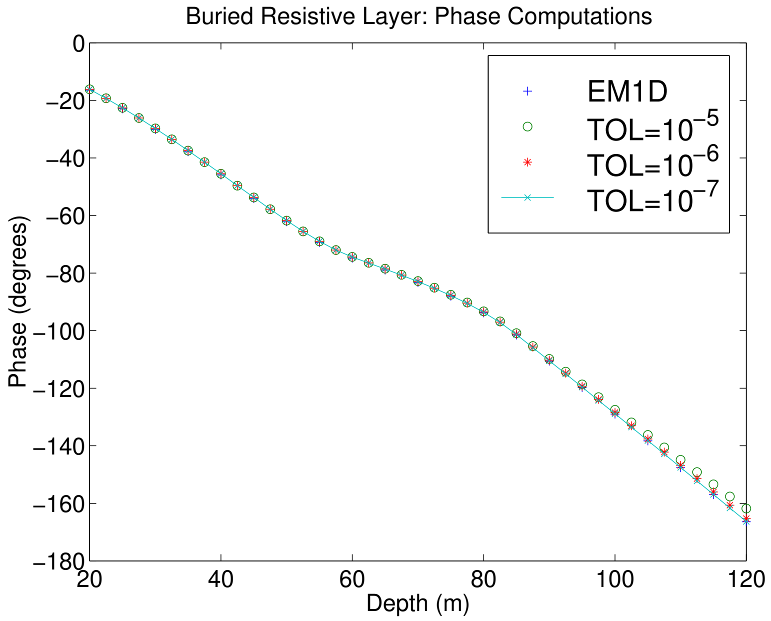


**FIG. 10.** Comparison of FDFD computed phase of magnetic field in the layered model with buried resistive layer in Fig. 8 with semianalytic results from EM1D of Ki-Ha Lee (LBNL). The smallest choice of convergence tolerance gives virtually the same results as EM1D for this example, while the other two are also in good agreement.

other parameters are the same including those used for the PML. The computation was performed as in the previous example and required approximately 3.3 hours of CPU time using about 1150 iterations to achieve convergence (with observed excellent agreement) for the intermediate choice of tolerance ($10^{-6}$). The smallest tolerance ($10^{-7}$) required about 7.5 hours and 2700 iterations. In Figs. 11 and 12 the results of the code calculations for the magnetic field magnitude and phase are again compared to results for the same model obtained using the code EM1D developed by Ki-Ha Lee at LBNL. The observed agreement is excellent for the two smallest choices of convergence tolerance, but the resistive background case clearly is harder to compute since the worst agreement seen here is for the phase at large depths when the largest choice of convergence tolerance ($10^{-5}$) was in use.

Finally, consider the geometry shown in Fig. 13, which depicts a conductive body buried within a homogeneous halfspace with a rectangular loop of current as the excitation. The frequency of operation is 1 kHz. The $x$ component of the electric field and the $z$ component of the magnetic field are sampled along the $y$ axis about the origin. The magnitude and phase of the electric field are shown in Figs. 14 and 15. The magnitude and phase of the magnetic field are displayed in Figs. 16 and 17. In each plot data from codes described in [10] are compared against data generated by FDFD. The three curves used in the comparisons to FDFD are: (a) IE for the full integral equation solution, (b) QRS for the quasi-linear approximation using the simplest scalar reflectivity tensor, and (c) QRD for the quasi-linear approximation using the diagonal reflectivity tensor. FDFD produces results similar to those obtained from IE, QRS, and QRD for both the electric and magnetic fields in all

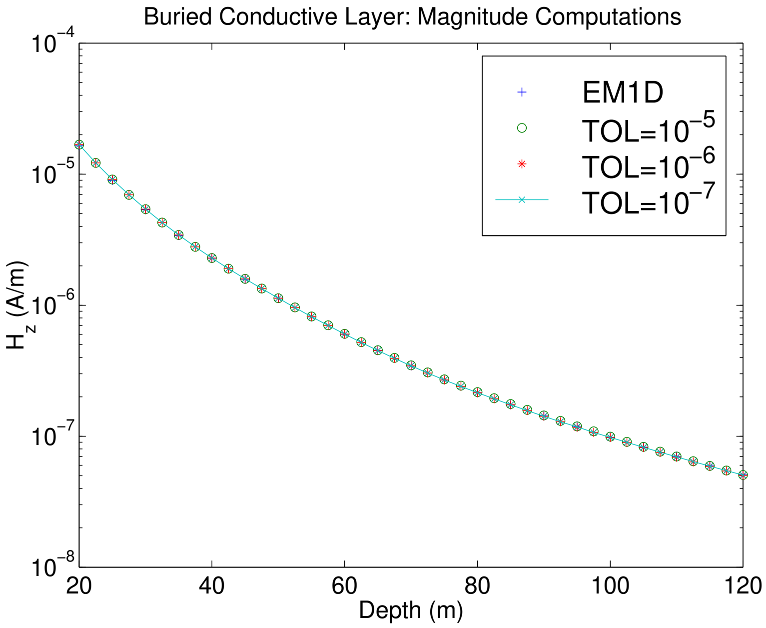


**FIG. 11.** Comparison of FDFD computed magnitude of magnetic field in the layered model with buried conductive layer as in Fig. 8 (but reversing the values 0.3 ↔ 0.016) with those from EM1D. All three choices of convergence tolerance give virtually the same results for this example, and are in good agreement with EM1D.

cases. FDFD is seen to be especially good at finding the dip in the magnetic field magnitude in Fig. 16 and at approximating the magnetic field phase in Fig. 17.

## 4. DISCUSSION

We continue to test and improve the EM forward modeling capability developed here with the ultimate goal of providing the forward modeling tools needed for a fully nonlinear inversion technique for electromagnetic induction tomography. Working in parallel, a new approach to the inverse problem of electromagnetics has been developed by [13] based on the so-called "adjoint technique." This method has the very useful property that the inverse problem can be solved approximately by making two uses of the same forward modeling code we have developed and described here. Using a somewhat oversimplified description of this technique, the updates to the electrical conductivity distribution are obtained by first making one pass through the forward solver using the latest best guess of the nature of the conducting medium, and then another pass with the adjoint operator (which for this problem is just the conjugate transpose of the forward modeling operator) applied to the differences in computed and measured data. (The adjoint method is modular when applied in this fashion and could make use of other forward solvers as long as they share the main features of the one described here.) Then the results of these two calculations are combined to determine updates to the original conductivity model. The resulting procedure is iterative and can be applied successively to parts of the data, *e.g.*, data associated with one transmitter location can be used to update the model before other transmitter locations are considered. This procedure

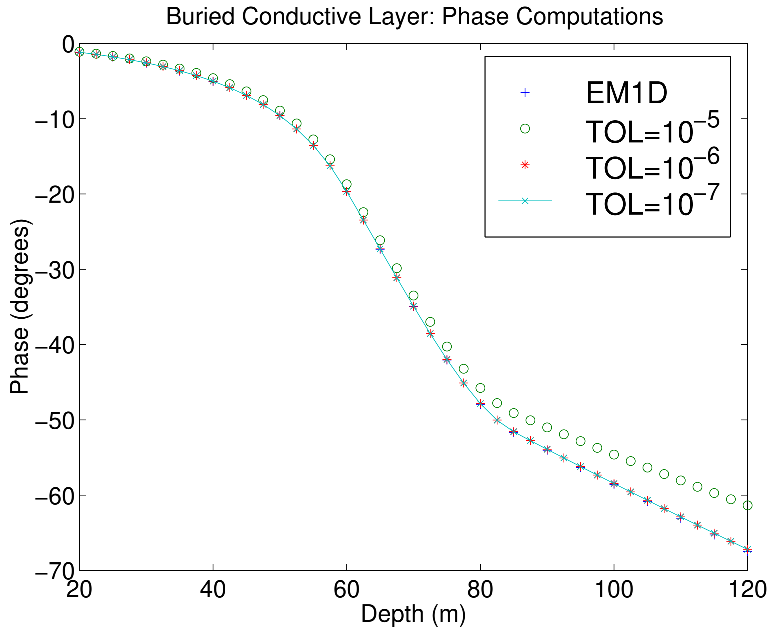


**FIG. 12.** Comparison of FDFD computed phase of magnetic field in the layered model with buried resistive layer in Fig. 8 (but reversing the values 0.3 ↔ 0.016) with those from EM1D. The largest deviation from EM1D is observed here for the largest choice of convergence tolerance, while the two smallest values give virtually the same results as EM1D for this example.

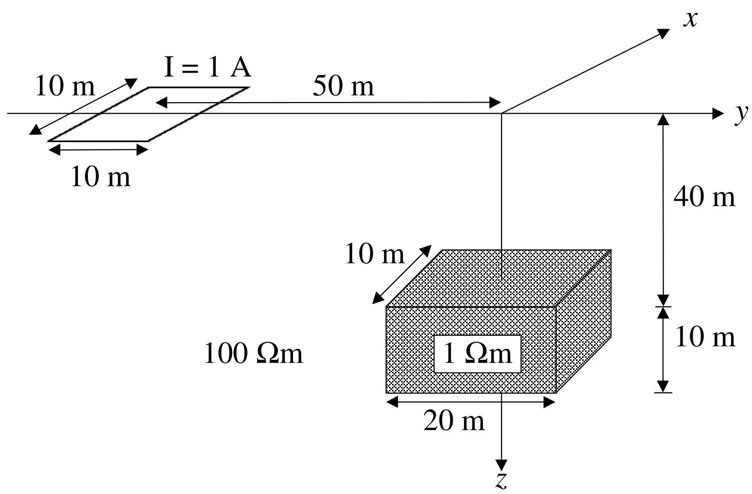


**FIG. 13.** Current loop at the surface of medium with a conductive body buried in a homogeneous halfspace as in [10]. The frequency of operation is 1 kHz.

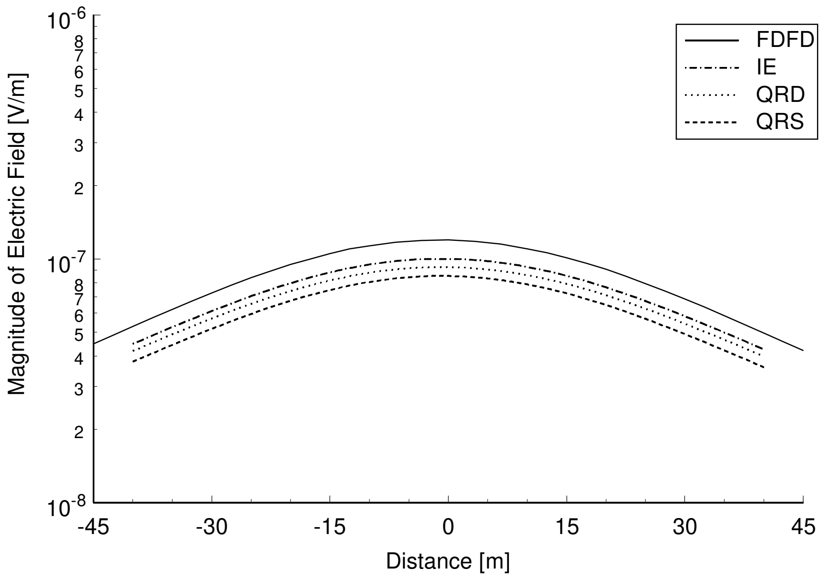


**FIG. 14.** Comparison of the scattered electric field magnitude for model in Figure 13. The fields are sampled along the $y$ axis about the origin.

has several of the same advantages as the very well tested method of wave equation migration in reflection seismology [14] and is also related to more recent methods in electromagnetics introduced by [15].

## APPENDIX

Various special symbols used in this paper will now be defined. First, $x_m$, $y_m$, and $z_m$ are the edge lengths of the $m$th cell (Fig. 1) in the $x$, $y$, and $z$ directions, respectively. Additional lengths associated with the magnetic fields (staggered grid cell lengths) are given by

$$\overline{x}_m = \frac{(x_m + x_d)}{2}, \overline{y}_m = \frac{(y_m + y_l)}{2}, \overline{z}_m = \frac{(z_m + z_f)}{2}. \tag{A.1}$$

Then, the area of the staggered grid cell face is given by

$$\begin{aligned} a_{m_x} &= \frac{y_m z_m + y_l z_l + y_f z_f + y_{lf} z_{lf}}{4}, \\ a_{m_y} &= \frac{x_m z_m + x_d z_d + x_f z_f + x_{df} z_{df}}{4}, \\ a_{m_z} &= \frac{x_m y_m + x_d y_d + x_l y_l + x_{dl} y_{dl}}{4} \end{aligned} \tag{A.2}$$

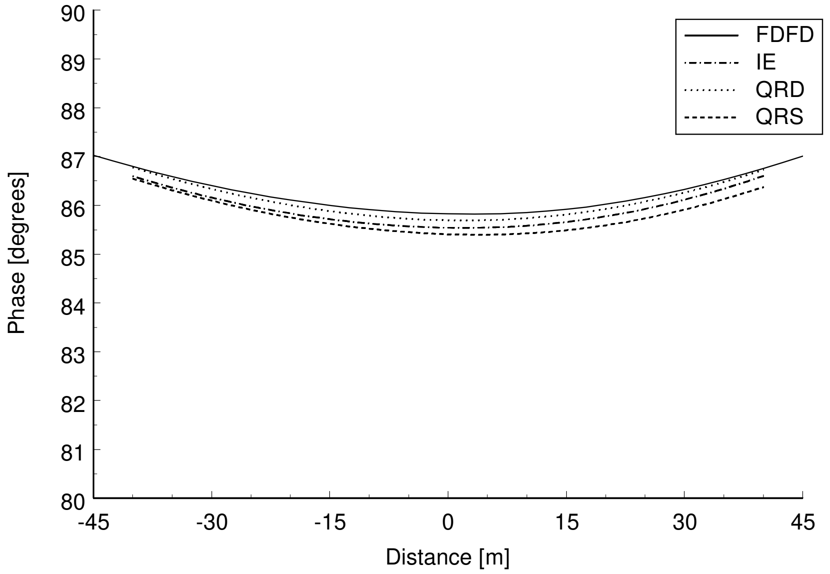


**FIG. 15.** Comparison of the scattered electric field phase for model in Figure 13. The fields are sampled along the $y$ axis about the origin.

in the $x$, $y$, and $z$ directions, respectively. Next, the permittivities associated with the electric field at an edge are given by

$$\begin{aligned}
\overline{\epsilon}_{m_{xx}} &= \frac{y_m z_m \epsilon_{m_{xx}} + y_l z_l \epsilon_{l_{xx}} + y_f z_f \epsilon_{f_{xx}} + y_{lf} z_{lf} \epsilon_{lf_{xx}}}{4}, \\
\overline{\epsilon}_{m_{yy}} &= \frac{x_m z_m \epsilon_{m_{yy}} + x_d z_d \epsilon_{d_{yy}} + x_f z_f \epsilon_{f_{yy}} + x_{df} z_{df} \epsilon_{df_{yy}}}{4}, \\
\overline{\epsilon}_{m_{zz}} &= \frac{x_m y_m \epsilon_{m_{zz}} + x_d y_d \epsilon_{d_{zz}} + x_l y_l \epsilon_{l_{zz}} + x_{dl} y_{dl} \epsilon_{dl_{zz}}}{4}.
\end{aligned} \tag{A.3}$$

And finally, the magnetic permeabilities associated with the magnetic field component at a face are given by

$$\begin{aligned}
\overline{\mu}_{m_{xx}} &= \frac{\mu_{m_{xx}} \mu_{d_{xx}} (x_m + x_d)}{(x_m \mu_{d_{xx}} + x_d \mu_{m_{xx}})}, \\
\overline{\mu}_{m_{yy}} &= \frac{\mu_{m_{yy}} \mu_{l_{yy}} (y_m + y_l)}{(y_m \mu_{l_{yy}} + y_l \mu_{m_{yy}})}, \\
\overline{\mu}_{m_{zz}} &= \frac{\mu_{m_{zz}} \mu_{f_{zz}} (z_m + z_f)}{(z_m \mu_{f_{zz}} + z_f \mu_{m_{zz}})}.
\end{aligned} \tag{A.4}$$

The set of all these cell quantities is represented using matrices as

$$\boldsymbol{D}_\ell = \mathrm{Diag}\left(\ldots, z_m, y_m, z_m, \ldots\right),$$

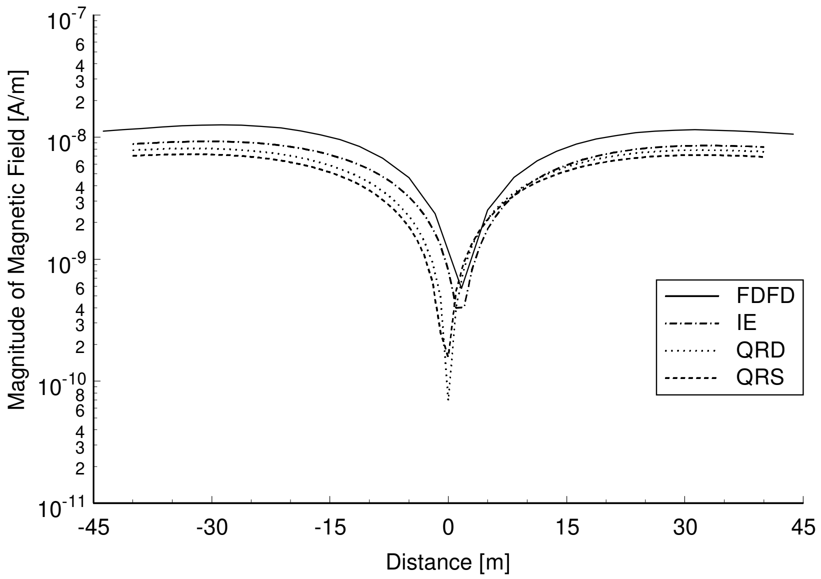


**FIG. 16.** Comparison of the scattered magnetic field magnitude for the model in Figure 13. The fields are sampled along the $y$ axis about the origin.

$$\boldsymbol{D}_{\bar{\ell}} = \mathrm{Diag}\left(\ldots, \overline{z}_m, \overline{y}_m, \overline{x}_m, \ldots\right), \tag{A.5}$$

$$\begin{aligned}\boldsymbol{D}_A &= \mathrm{Diag}\left(\ldots, x_m y_m, x_m z_m, y_m z_m, \ldots\right), \\ \boldsymbol{D}_{\bar{A}} &= \mathrm{Diag}\left(\ldots, a_{m_z}, a_{m_y}, a_{m_x}, \ldots\right),\end{aligned} \tag{A.6}$$

$$\begin{aligned}\boldsymbol{D}_{A\epsilon} &= \mathrm{Diag}\left(\ldots, \overline{\epsilon}_{m_{zz}}, \overline{\epsilon}_{m_{yy}}, \overline{\epsilon}_{m_{xx}}, \ldots\right), \\ \boldsymbol{D}_{\mu} &= \mathrm{Diag}\left(\ldots, \overline{\mu}_{m_{zz}}, \overline{\mu}_{m_{yy}}, \overline{\mu}_{m_{xx}}, \ldots\right).\end{aligned} \tag{A.7}$$

Additionally, the volume matrix is given by

$$\boldsymbol{D}_{V\epsilon\epsilon} = \mathrm{Diag}\left(\ldots, V_{m_z}, V_{m_y}, V_{m_x}, \ldots\right), \tag{A.8}$$

where

$$\begin{aligned}V_{m_\alpha} = \\ &\frac{1}{8}\Big[\left|\epsilon_{m_{\alpha\alpha}}\right|^2 x_m y_m z_m + \left|\epsilon_{d_{\alpha\alpha}}\right|^2 x_d y_d z_d + \\ &\left|\epsilon_{l_{\alpha\alpha}}\right|^2 x_l y_l z_l + \left|\epsilon_{f_{\alpha\alpha}}\right|^2 x_f y_f z_f +\end{aligned}$$

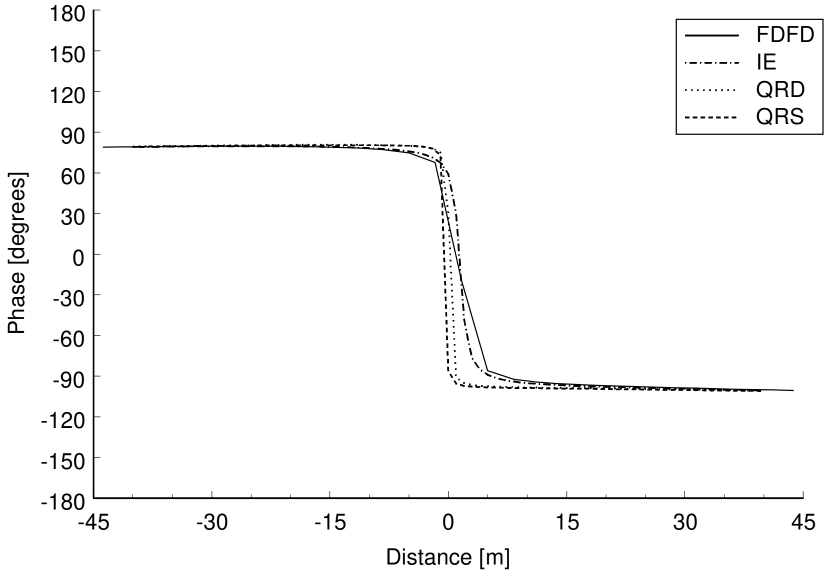


**FIG. 17.** Comparison of the scattered magnetic field phase for model in Figure 13. The fields are sampled along the $y$ axis about the origin.

$$\begin{aligned}&\left|\epsilon_{df_{\alpha\alpha}}\right|^2 x_{df}y_{df}z_{df} + \left|\epsilon_{dl_{\alpha\alpha}}\right|^2 x_{dl}y_{dl}z_{dl} + \\ &\left|\epsilon_{lf_{\alpha\alpha}}\right|^2 x_{lf}y_{lf}z_{lf} + \left|\epsilon_{dlf_{\alpha\alpha}}\right|^2 x_{dlf}y_{dlf}z_{dlf}\Big] .\end{aligned} \tag{A.9}$$

The vectors $\vec{e}$, $\vec{h}$, $\vec{j}$, and $\vec{m}$ have the general form

$$\vec{f} = \left(\ldots, F_{m_z}, F_{m_y}, F_{m_x}, \ldots\right) . \tag{A.10}$$

Finally, the coefficient matrices $\boldsymbol{A}$ and $\boldsymbol{B}$ are given as in [16] by (note that the first row displayed in each of the two following equations is shown to clarify the indexing scheme used in the matrix shown)

$$\begin{array}{cc} & \begin{array}{ccccccccccccccc} \ldots & z_m & y_m & x_m & z_u & y_u & x_u \ldots & z_r & y_r & x_r & \ldots & z_b & y_b & x_b \ldots \end{array} \\ \boldsymbol{A} = & \left[\begin{array}{cccccccccccccc} \ddots & & & & & & & & & & & & & \\ & 0 & -1 & 1 & 0 & 1 & 0 & \ldots & 0 & 0 & -1 & \ldots & 0 & 0 & 0 \\ & 1 & 0 & -1 & -1 & 0 & 0 & \ldots & 0 & 0 & 0 & \ldots & 0 & 0 & 1 \\ & -1 & 1 & 0 & 0 & 0 & 0 & \ldots & 1 & 0 & 0 & \ldots & 0 & -1 & 0 \\ & & & & & \ddots & & & & & & & & \end{array}\right] \end{array} \tag{A.11}$$

and

$$
\boldsymbol{B} = \begin{array}{c}
\begin{array}{cccccccccc} \cdots & z_f & \cdots & y_l & \cdots & x_d & z_m & y_m & x_m & \cdots \end{array} \\
\begin{bmatrix}
\ddots & & & & & & & & & \\
 & 1 & & & & & & & & \\
 & & \ddots & & & & & & & \\
 & & & 1 & & & & & & \\
 & & & & \ddots & & & & & \\
 & & & & & 1 & & & & \\
 & -1 & \ldots & -1 & \ldots & -1 & 1 & 1 & 1 & \\
 & -1 & \ldots & -1 & \ldots & -1 & 1 & 1 & 1 & \\
 & -1 & \ldots & -1 & \ldots & -1 & 1 & 1 & 1 & \\
 & & & & & & & & & \ddots
\end{bmatrix}
\end{array}. \tag{A.12}
$$

## ACKNOWLEDGMENTS

We thank J. B. Grant and R. M. Sharpe for helping to establish the directions we would take in the EM forward modeling code development for this problem. Also, our thanks to M. S. Zhdanov and E. Tartaras for providing us with some numerical data from the codes described in [10].

## REFERENCES

1. W. M. Telford, L. P. Geldart, R. E. Sheriff, and D. A. Keys, *Applied Geophysics*, Cambridge University Press, Cambridge, England, 1976, Section 3.5.4.
2. A. Ramirez, W. D. Daily, D. LaBrecque, E. Owen, and D. Chesnut, Monitoring an underground steam injection process using electrical resistance tomography, *Water Resources Res. 29*, 73–87, 1993.
3. H.-W. Tseng, A. Becker, M. J. Wilt, and M. Deszcz-Pan, “A borehole-to-surface electromagnetic survey,” *Geophysics* **73**, 1565–1572, 1998.
4. M. S. Zhdanov, I. M. Varentsov, J. T. Weaver, N. G. Golubev, and V. A. Krylov, “Methods for modeling electromagnetic fields: Results from COMMEMI — The international project on the Comparison Of Modeling Methods for ElectroMagnetic Induction,” *J. Appl. Geophys.* **37**, 133–271, 1997.
5. K. Beilenhoff, W. Heinrich, and H. L. Hartnagel, “Improved finite-difference formulation in frequency domain for three-dimensional scattering problems,” *IEEE Trans. Microwave Theory Tech.* **40**, 540–546, 1992.
6. J. P. Berenger, “A perfectly matched layer for the absorption of electromagnetic waves,” *J. Computational Phys.* **114**, 185–200, 1994.
7. J. Y. Wu, D. M. Kingsland, J. F. Lee, and R. Lee, “A comparison of anisotropic PML to Berenger’s PML and its application to the finite-element method for EM scattering,” *IEEE Trans. Antennas Propagat.* **45**, 40–50, 1997.
8. Z. S. Sacks, D. M. Kingsland, R. Lee, and J. F. Lee, “A perfectly matched anisotropic absorber for use as an absorbing boundary condition,” *IEEE Trans. Antennas Prop.* **43**, 1460–1463, 1995.
9. M. Kuzuoglu and R. Mittra, “Frequency dependence of the constitutive parameters of causal perfectly matched anisotropic absorbers,” *IEEE Microwave Guided Wave Lett.* **6**, 447–449, 1996.
10. M. S. Zhdanov and S. Feng, “Quasi-linear approximation in 3D electromagnetic modeling,” *Geophysics* **61**, 646–665, 1996.
11. T. T. Wu and R. W. P. King, “The cylindrical antenna with nonreflecting resisitive loading,” *IEEE Trans. Antennas Prop.* **13**, 369–373, 1965.

12. N. J. Champagne, J. T. Williams, R. M. Sharpe, S. U. Hwu, and D. R. Wilton, "Numerical modeling of impedance loaded multi-arm archimedian spiral antennas," *IEEE Trans. Antennas Prop.* **40**, 102–108, 1992.

13. O. Dorn, H. Bertete-Aguirre, J. G. Berryman, and G. C. Papanicolaou, "A nonlinear inversion method for 3D-electromagnetic imaging using adjoint fields," *Inverse Problems*, submitted June, 1999.

14. J. F. Claerbout, *Fundamentals of Geophysical Data Processing: With Applications to Petroleum Prospecting*, McGraw-Hill, New York, 1976.

15. M. S. Zhdanov, P. Traynin, and J. R. Booker, "Underground imaging by frequency-domain electromagnetic migration," *Geophysics* **61**, 666–682, 1996.

16. N. J. Champagne, J. G. Berryman, H. M. Buettner, J. B. Grant, and R. M. Sharpe, "A finite-difference frequency-domain code for electromagentic induction tomography," *SAGEEP Conference Proceedings*, Oakland, California, March 14–18, 1999, pp. 931–940.